

# Physics-Informed Neural State-Space Modeling of Battery-Electric Vehicle Dynamics for Closed-Loop Automated Parking Simulation

Sirong Pan, Guannan Tian, and Pan Song

**Abstract**—This paper contributes to vehicle dynamics modeling by introducing a physics-informed neural state-space model tailored for the parking regime of a production battery-electric sedan, identified entirely from field-test maneuvers. At parking speeds the model captures what the kinematic idealization omits, including actuator lag, drivetrain creep, brake-hold transitions through standstill, and frequent reversals of the motion direction. A gear-conditioned velocity constraint is imposed during training, and the yaw rate is read out as a learned residual on a kinematic-bicycle prior, so that the network devotes its capacity to the deviation from physics rather than to its reproduction. These training-time physics make the customary inference-time state limiter redundant. The commanded-to-actual behavior of the drive, brake, and steering actuators is reproduced by dedicated submodels, for which signal fidelity proves an unreliable proxy for closed-loop value; tuning the brake on its velocity consequence rather than on its own signal reverses the verdict reached at the signal level. The model generalizes to held-out maneuvers in fully open-loop simulation, and, despite being identified from only 16 field tests, the assembled command-to-vehicle chain earns Good ratings on the vehicle states under the ISO/TS 18571 objective rating metric. Embedded as the real-time plant of an interactive simulator, it enables a production-representative planning stack to park the vehicle through the learned dynamics. This makes the model suitable for pre-calibrating an automated-parking planning and control stack in the virtual development phase without the manufacturer's proprietary chassis and actuator parameters.

**Index Terms**—Automated parking, electric vehicles, model-in-the-loop simulation, neural state-space models, physics-informed neural networks, system identification, vehicle dynamics.

## I. INTRODUCTION

Accurate vehicle dynamics modeling is fundamental to the development, tuning, and evaluation of automated driving functions, including automated parking. The parking regime, however, is poorly served by established modeling practice. At speeds below walking pace the classical dynamics models collapse to kinematics, yet the real behavior is dominated by the effects those kinematics discard: actuator lag and

hysteresis, the creep torque of an electric driveline, brake-hold transitions through standstill, and frequent reversals of the motion direction. Production practice nonetheless adopts the kinematic-bicycle model for planning, where it is appropriate, and for execution-level simulation, where it idealizes away the phenomena that decide whether a maneuver lands in the bay.

Data-driven modeling avoids this idealization. Neural networks learn vehicle dynamics from real-vehicle measurements [1]–[4], neural state-space and continuous-time formulations cast system identification as the learning of compact state and output maps [5]–[7], and physics-informed or hybrid models constrain the learned dynamics toward physical plausibility [8]–[10]. Across this literature, however, the model is almost always judged by open-loop prediction accuracy on forward-driving data, and almost never in the role it is built to fill, as the executed plant inside a closed planning and control loop. A model accurate one step ahead can still fail as a closed-loop plant, where errors compound, the controller reacts to the model's own outputs, and evaluation must run in real time. For a parking plant, on which a production planner is tuned and validated, this closed-loop fidelity, not the open-loop residual, determines whether the model is usable.

Two further gaps are specific to parking. Its dynamics involve signed velocities and gear-conditioned transitions among reverse, drive, and standstill that forward-driving formulations do not represent, and the commanded-to-actual transfer of the production actuators, which dominates the response at parking speeds, is rarely modeled. The precursor to this work [4] introduced a neural state-space (NSS) model of forward-driving dynamics and identified parking as the open extension. Automated-parking motion planning is itself mature [11], [12], but it is developed against the kinematic idealization rather than a high-fidelity learned plant of the target vehicle.

These gaps weigh most on the teams that develop automated-parking software, which must calibrate planning and control against vehicle dynamics that the manufacturer seldom releases in parametric form and that are costly to characterize on a prototype. This paper develops, analyzes, and deploys a physics-informed NSS model of the parking-regime dynamics of a production battery-electric sedan, identified entirely from 16 field-test maneuvers and validated in the role it is meant to serve, as the real-time plant inside an interactive parking simulator through which a production-representative planning stack parks the vehicle. The contributions are four-fold:

- 1) a parking-capable NSS formulation combining a gear-conditioned, three-branch velocity constraint with a physics-residual yaw-rate readout, whose training-time

Manuscript received XX XX, 2026. This work was supported by the Wuhu Intelligent Logistics Technology Research and Development Center under Grant WHSYFZX202402. (Corresponding author: Pan Song.)

S. Pan is with the Modern Logistics and Intelligent Manufacturing College, Wuhu Vocational Technical University, Wuhu 241003, Anhui, China (e-mail: 900289@whit.edu.cn).

G. Tian is with the Department of Vehicle Engineering, Nanjing University of Aeronautics and Astronautics, Nanjing 210016, China (e-mail: tianguannan@nuaa.edu.cn).

P. Song is with the Kaiyang Laboratory, Chery Automobile Co., Ltd., Wuhu 241009, Anhui, China (e-mail: songpan14@gmail.com; ORCID: 0000-0003-0814-6824).

The source code and trained models are available at <https://github.com/pansong/PyNSSM-Parking>, and the parking simulator at <https://github.com/pansong/auto-parking-sim>.

physics render the customary inference-time state limiter redundant;

- 2) an actuator modeling study across five architectures and three state-input variants per channel, showing that open-loop signal fidelity does not predict closed-loop value, that state dependence differs across channels, and that consequence-tuning the selected submodel, by back-propagation through the frozen vehicle model, reverses the verdict against long-memory architectures;
- 3) a closed-loop deployment in which a production-representative planning stack parks the vehicle through the learned dynamics over a deterministic 36-cell scenario grid and a 252-cell held-out robustness grid, with the controller-induced clearance trade reported;
- 4) a small-data experimental methodology comprising stratified cross-validation, a leave- $r$ -repeats-out learning curve, seed-noise decomposition, and sensor-blind-zone-masked metrics, by which each design choice is either supported by a controlled comparison exceeding the measured noise floor or resolved by simplicity.

The rest of this paper is organized as follows. Section II presents the physics-informed NSS model. Section III develops the per-channel actuator submodels and their physical envelopes. Section IV details the field-test data, the training and evaluation protocol, and the simulator deployment. Section V reports the open-loop validation, the limiter comparison, the design ablations, the actuator study, the standardized fidelity assessment, and the closed-loop evaluation. Section VI concludes.

## II. PHYSICS-INFORMED NEURAL STATE-SPACE MODEL

### A. Neural State-Space Formulation

Following the reduced-order strategy established in [4], the parking-regime dynamics of the test vehicle are represented within a neural state-space framework. The state vector  $\mathbf{x} = [v_x \ \omega_z]^T$  comprises the longitudinal velocity and the yaw rate, and the output vector  $\mathbf{y} = [a_x \ a_y]^T$  collects the longitudinal and lateral accelerations measured by the onboard inertial sensor. The input vector

$$\mathbf{u} = [d_g \ \tau_m \ p_b \ \delta_{sw}]^T \quad (1)$$

consists of the gear state  $d_g \in \{-1, 0, +1\}$  for reverse, neutral/park, and drive, respectively; the motor torque  $\tau_m$ ; the brake master-cylinder pressure  $p_b$ ; and the steering-wheel angle  $\delta_{sw}$ . The zero level merges neutral and park deliberately. The recorded gear signal encodes both identically, and the two are dynamically equivalent within the modeled states: neither transmits tractive torque, and both occur only at standstill, where the parking pawl's mechanical lock acts entirely inside the wheel-speed sensor blind zone. Their distinct deployment semantics are restored by the command interface of Section IV-C. Note that these are the actual actuator responses recorded on the vehicle bus rather than the controller commands; the commanded-to-actual transfer is modeled separately by the per-channel actuator submodels of Section III, which permits the two model families to be

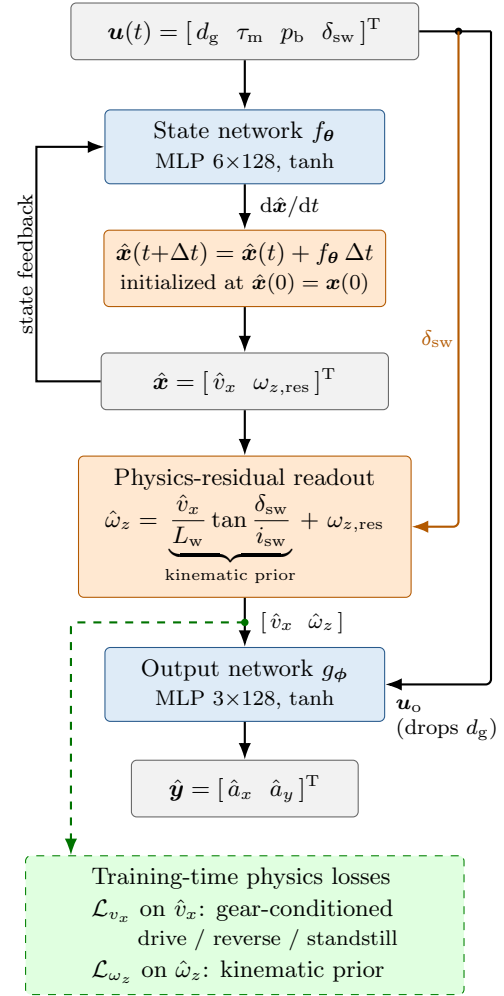


Fig. 1. Architecture of the physics-informed neural state-space model, with state  $\hat{\mathbf{x}} = [\hat{v}_x \ \hat{\omega}_z]^T$  and yaw-rate readout  $\hat{\omega}_z = \omega_{z,ref} + \omega_{z,res}$ . Blue blocks denote learned networks, orange blocks deterministic operations, gray blocks signals, and the dashed green band the physics-informed losses, which act at training time only.

identified and validated independently before being chained in closed loop.

The NSS model comprises two principal components, a state network  $f_\theta$  and an output network  $g_\phi$ , each structured as a fully connected multi-layer perceptron (MLP) with hyperbolic-tangent activations. At each time step, the state network computes the time derivative of the state rather than the next state directly; this derivative is then integrated by the forward-Euler rule at the field-test sampling interval  $\Delta t = 10$  ms:

$$\hat{\mathbf{x}}(0) = \mathbf{x}(0), \quad (2a)$$

$$\hat{\mathbf{x}}(t + \Delta t) = \hat{\mathbf{x}}(t) + f_\theta(\hat{\mathbf{x}}(t), \mathbf{u}(t)) \Delta t, \quad (2b)$$

$$\hat{\mathbf{y}}(t) = g_\phi(\hat{\mathbf{x}}(t), \mathbf{u}_o(t)), \quad (2c)$$

where  $f_\theta$  and  $g_\phi$  denote the state and output networks with trainable parameters  $\theta$  and  $\phi$ , respectively;  $\hat{\mathbf{x}}(t)$  and  $\hat{\mathbf{y}}(t)$  are the predicted state and output at time  $t$ ; the initial prediction  $\hat{\mathbf{x}}(0)$  is set to the true initial state  $\mathbf{x}(0)$ ;  $\Delta t$  is the integration step size; and the output-branch input  $\mathbf{u}_o = [\tau_m \ p_b \ \delta_{sw}]^T$  excludes the gear state, whose influence is already encapsulated

in the evolution of  $\hat{\mathbf{x}}$ . All subsequent predictions follow from (2b) in a purely open-loop manner, with no measured state fed back during inference, so that every reported metric reflects multi-step rollout accuracy over the complete maneuver. The state network employs six hidden layers of 128 units and the output network three; the selection of this capacity is revisited empirically in Section V.

All channels are scaled to  $[-1, 1]$  by min-max normalization computed on the training set only. In contrast to [4], each channel is first clipped to its 0.5th–99.5th percentile range, which prevents rare actuator transients from compressing the effective resolution of the remaining samples while keeping the scaled signals bounded and therefore compatible with the saturating activations. The data-fidelity losses are mean absolute errors on the scaled states and outputs; the velocity component of the state loss is masked wherever the measured speed falls inside the wheel-speed sensor blind zone of Section IV,  $|v_x| < 0.5$  km/h, within which the reference signal carries no usable information.

### B. Physics-Residual Yaw-Rate Readout

At parking speeds, tire slip is negligible and the yaw rate is governed almost entirely by kinematics: on the field-test data, the kinematic-bicycle relation

$$\omega_{z,\text{ref}} = \frac{v_x}{L_w} \tan\left(\frac{\delta_{\text{sw}}}{i_{\text{sw}}}\right) \quad (3)$$

explains the measured yaw rate with a coefficient of determination of 0.997, where  $\omega_{z,\text{ref}}$  denotes the kinematic reference yaw rate;  $L_w = 3.0$  m the wheelbase; and  $i_{\text{sw}} = 12.1$  the steering ratio. Such a strong prior is exploited structurally rather than discarded: the state network integrates the residual yaw rate  $\omega_{z,\text{res}}$  as its second state, so the internal state of (2b) becomes  $\hat{\mathbf{x}} = [\hat{v}_x \ \omega_{z,\text{res}}]^T$ , and the observed yaw rate is reconstructed at readout as

$$\hat{\omega}_z(t) = \omega_{z,\text{ref}}(\hat{v}_x(t), \delta_{\text{sw}}(t)) + \omega_{z,\text{res}}(t), \quad (4)$$

with the initial residual decomposed consistently from (2a) as  $\omega_{z,\text{res}}(0) = \omega_z(0) - \omega_{z,\text{ref}}(0)$ . The reconstruction (4) is applied wherever the yaw rate is consumed, namely the output network input, the physics-informed losses, and all evaluation metrics; in particular, the output network in (2c) receives the reconstructed pair  $[\hat{v}_x \ \hat{\omega}_z]^T$  rather than the internal state, as depicted in Fig. 1. The network capacity is thereby devoted exclusively to the small slip- and compliance-induced deviation from the kinematic ideal. This structural prior reduces the validation velocity error by approximately 27% relative to an otherwise identical model that predicts the yaw rate directly, an ablation reported in Section V-C.

### C. Gear-Conditioned Physics-Informed Losses

The parent model [4] addresses forward driving only. Parking maneuvers, in contrast, are dominated by direction changes: the velocity is negative in reverse, positive in drive,

and pinned at standstill between the two. The physical direction constraint is therefore imposed during training as a soft, gear-conditioned loss with three mutually exclusive branches:

$$\begin{aligned} \mathcal{L}_{v_x} = \mathbb{E} & \left[ \mathcal{I}(d_g > 0.5) \max(0, -\hat{v}_x) \right. \\ & + \mathcal{I}(d_g < -0.5) \max(0, \hat{v}_x) \\ & \left. + \mathcal{I}(|d_g| \leq 0.5) |\hat{v}_x| \right], \end{aligned} \quad (5)$$

where  $\mathbb{E}[\cdot]$  denotes the expectation over the training samples,  $\mathcal{I}(\cdot)$  the indicator function, and all quantities are evaluated in the scaled space. The drive and reverse branches penalize only direction violations, leaving the velocity magnitude unconstrained, whereas the zero-gear branch anchors the velocity toward standstill, reflecting that the test vehicle occupies neutral or park only at rest. A second soft loss attracts the yaw-rate prediction toward the kinematic prior,

$$\mathcal{L}_{\omega_z} = \mathbb{E} \left[ |\hat{\omega}_z - \omega_{z,\text{ref}}| \right], \quad (6)$$

and the total training objective combines the masked data losses with the two physics terms,

$$\mathcal{L} = \mathcal{L}_{\mathbf{x}}^{\text{masked}} + \mathcal{L}_{\mathbf{y}} + \lambda_{v_x} \mathcal{L}_{v_x} + \lambda_{\omega_z} \mathcal{L}_{\omega_z}, \quad (7)$$

where  $\mathcal{L}_{\mathbf{x}}^{\text{masked}}$  and  $\mathcal{L}_{\mathbf{y}}$  are the masked state and output data-fidelity losses, and  $\lambda_{v_x}$  and  $\lambda_{\omega_z}$  weight the velocity and yaw-rate physics terms. The weights  $\lambda_{v_x} = 0.1$  and  $\lambda_{\omega_z} = 0.5$  are fixed by physical reasoning and simplicity rather than by tuning: in the hyperparameter sweep their effect was weak relative to the seed-noise floor, so, following the selection discipline of Section IV-B, the heavier yaw weight reflects the high reliability of the kinematic prior it enforces, while the lighter velocity weight imposes only a soft direction-and-standstill constraint. The question of whether a hard state limiter retains any value at inference time is then settled empirically in Section V-B.

## III. PER-CHANNEL ACTUATOR MODELS

The NSS model of Section II consumes the actual actuator responses, whereas a parking controller issues commands. In [4], the two were treated as identical, which is acceptable for offline replay but precludes closed-loop simulation: under a controller in the loop, the lag, gain, and saturation of each actuator shape the vehicle response and the controller's reaction to it. The field-test vehicle records both sides of this transfer on its bus, which enables the commanded-to-actual dynamics to be identified explicitly and chained in front of the NSS model; Fig. 2 depicts the deployed chain. The decomposition also carries a practical commitment beyond fidelity: each channel can be re-identified in isolation when its subsystem is recalibrated, a property examined together with the monolithic alternative in Section V-D.

### A. Channels and Candidate Architectures

Three actuator channels are modeled, supplying the components  $\tau_m$ ,  $p_b$ , and  $\delta_{\text{sw}}$  of the NSS input vector (1), with commanded quantities distinguished from the recorded actuals by an asterisk. The drive channel maps the torque command

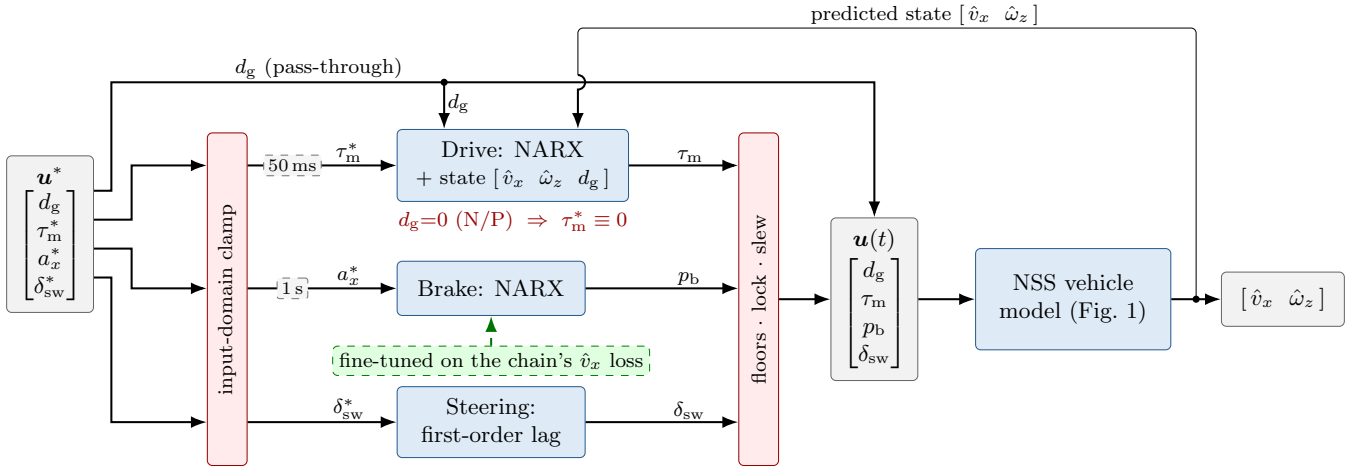


Fig. 2. Command-to-vehicle chain in deployed configuration. Controller commands pass the input-domain clamp, the per-channel actuator submodels, and the physical output envelope to form the actual input vector  $\mathbf{u}(t)$  of the NSS vehicle model. Dashed buffers mark the command histories the drive and brake submodels consume; the gear state passes through unclamped and also feeds the drive submodel. The green dashed element acts at training time only, fine-tuning the brake submodel on the chain's velocity loss, Section V-D. Asterisks denote commanded quantities; blue blocks denote identified models, red physical envelopes and hard interface rules, and gray signals.

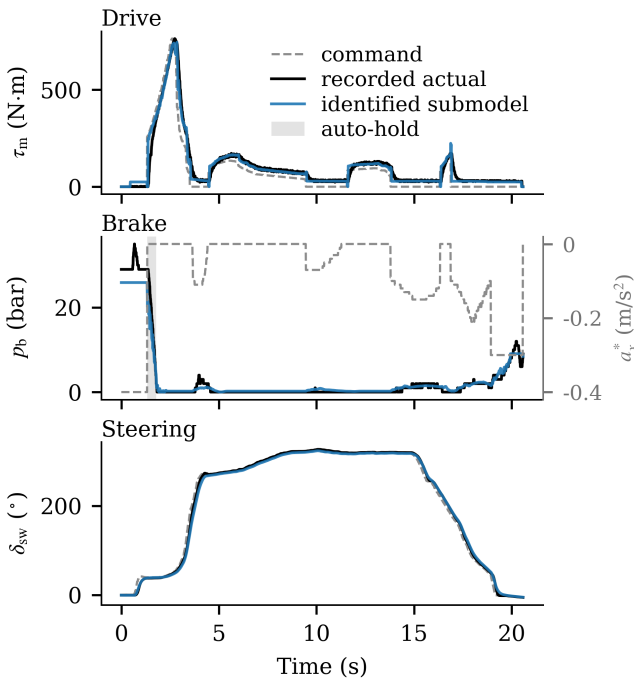


Fig. 3. Commanded-to-actual transfer of the deployed actuator channels over a complete held-out park-out maneuver, showing the commanded signal, the recorded actual response, and the identified submodel of each channel replayed open loop. The shaded region marks the auto-hold pressure released at launch.

to the actual motor torque,  $\tau_m^* \rightarrow \tau_m$ . The brake channel maps the deceleration command directly to the master-cylinder pressure,  $a_x^* \rightarrow p_b$ ; a cascade through the intermediate booster rod stroke was examined but not adopted, the rod stroke proving weakly informative about the resulting pressure. The steering channel maps the steering-wheel angle request to the actual steering-wheel angle,  $\delta_{sw}^* \rightarrow \delta_{sw}$ . Figure 3 illustrates each commanded-to-actual transfer on a held-out maneuver,

together with its reproduction by the per-channel candidates ultimately selected in Section V-D, replayed through the deployed physical envelopes. Residual mismatches remain visible on the drive channel, a small standstill offset and a release tail, but their closed-loop cost is bounded by the end-to-end accounting of Section V-D.

One property of the brake channel shapes its modeling. Beyond the commanded path, the recorded pressure carries an autonomous auto-hold component that no command explains. Decided by unobserved chassis logic, these holds appear in Fig. 3 as the shaded pressure at launch, and no command-driven candidate reproduces them, but the omission is tolerable, the deployed simulator regenerating hold-class pressure by commanding deceleration at every stop (Section IV-C). Their slow release nonetheless exceeds the 50 ms window of the identification-stage submodel, the reason the deployed brake carries a 1 s window, with long-memory architectures, a long short-term memory (LSTM) [13] network and a longer-window nonlinear autoregressive with exogenous inputs (NARX) [14] model, evaluated in Section V-D.

For every channel, five candidate architectures spanning three orders of magnitude in parameter count are fitted, with  $u^*$  and  $y$  denoting the channel's scalar command and actual response, respectively:

- 1) a first-order lag,  $\tau_1 \dot{y} = u^* - y$ , with a single learnable time constant;
- 2) a second-order lag parameterized by  $(\tau_2, \zeta, K)$ , capturing inertia and damping of hydraulic components;
- 3) a Hammerstein model, in which a small static nonlinearity  $\psi(u^*)$ , a  $1 \times 8 \times 8 \times 1$  perceptron, precedes a first-order lag, accommodating dead zones and saturation;
- 4) a NARX perceptron operating on the command and five lagged samples, 50 ms of history;
- 5) a gated recurrent unit (GRU) [15] with a 16-dimensional hidden state.

Each candidate is additionally fitted in three input variants:

command history only; command history plus physically motivated state features, such as vehicle speed and gear for the drive channel; and command history plus a uniform state interface  $[v_x \ \omega_z \ d_g]$  shared by all channels. Whether an actuator submodel benefits from vehicle-state inputs is thereby treated as an experimental question rather than a design assumption, and Section V-D shows the answer differs across channels.

### B. Physical Input–Output Envelopes

In closed-loop operation a controller may issue commands outside the domain spanned by the field tests, where a learned model extrapolates without physical grounding. All deployed submodels are therefore wrapped in physical envelopes derived from the data and the vehicle specification: commands are clamped to the identified input domains, for instance the deceleration command  $a_x^*$  to  $[-0.8, 0]$  m/s<sup>2</sup>, while outputs observe the physical floors, with torque and pressure non-negative, the steering lock of  $\pm 400^\circ$ , and a steering rate limited just above the highest slew rate observed in the field tests so the guard acts only on out-of-domain requests. A stress study in Section V-D examines which envelope regulates the chain. The recorded actuals are quantized to 2 N·m and 1 bar, setting a noise floor below which fidelity differences are not meaningful.

### C. Two-Phase Selection With Closed-Loop Fine-Tuning

Candidate selection proceeds in two phases. Phase A scores every channel–architecture–variant combination against the recorded actuals on held-out trials, by mean squared error (MSE), mean absolute error (MAE), and step-response metrics, and shortlists per channel. Phase B substitutes each shortlisted candidate into the complete chain, from controller commands through the submodel into the NSS rollout, and selects per-channel winners by the resulting vehicle-state accuracy; because submodel errors interact through the vehicle state, the assembled chain with all submodels active is the final authority. The protocol closes with an optional consequence-level stage that fine-tunes a selected submodel by backpropagating the chain’s vehicle-state loss through the frozen vehicle model into its weights, weighing each actuator error by its closed-loop effect rather than its signal proximity. A state-aware winner, fitted with measured states but deployed with NSS-predicted ones, is additionally fine-tuned for a short schedule on streams in which the frozen NSS supplies the state features, closing the identification-to-deployment gap without altering the NSS.

## IV. EXPERIMENTAL SETUP

### A. Test Vehicle and Field Test Data

The test vehicle is a battery-electric sedan, the EXEED Sterra ES, equipped with a production automated parking system. Its geometry enters the model as fixed constants: wheelbase  $L_w = 3.0$  m, track width 1.695 m, steering-wheel lock  $\pm 400^\circ$ , and steering ratio  $i_{sw} = 12.1$ . The rack is mildly nonlinear, about 13 near center and 12.1 toward the lock, and

the adopted value of 12.1 is corroborated by an independent least-squares fit of (3) to the field-test data, which yields 12.0.

A total of 16 parking trials were recorded at 100 Hz over the in-vehicle network, organized as four maneuver classes with four repetitions each: multi-segment park-in maneuvers containing reverse driving and gear reversals, and single-segment park-out maneuvers, each toward the left and the right. Trial lengths range from roughly 21 to 64 s. Every trial captures the complete command–response pairs of Section III alongside the vehicle states and accelerations, which enables the actuator submodels and the vehicle model to be identified from the same data. One sensor property shapes the entire evaluation methodology. The wheel-speed-derived velocity cannot resolve magnitudes below approximately 0.5 km/h, inside which the recorded signal is quantization noise rather than measurement. Parking maneuvers spend a substantial fraction of their duration at or near standstill, so naive error metrics would largely score the reproduction of sensor noise; all velocity losses and headline metrics in this paper are therefore masked to the moving region  $|v_x| \geq 0.5$  km/h.

### B. Training and Evaluation Protocol

1) *Training Configuration*: Each trial is tiled into end-aligned windows of 2121 samples, the shortest trial length, yielding 29 training sequences that jointly cover approach, transition, and standstill phases. The networks are trained for the full windows by backpropagation through the open-loop rollout (2b), with the Adam optimizer under a cosine learning-rate schedule starting at  $2 \times 10^{-3}$ , mean-absolute-error data losses, and the physics terms of (7). All models are implemented in PyTorch and trained on a single NVIDIA RTX A4500 GPU under the Windows Subsystem for Linux (WSL2). A convergence probe (Fig. 4) places the validation optimum near 3000 epochs, beyond which the held-out error stagnates or mildly degrades, so deployment fits are capped at 3200 epochs with continuous best-checkpoint tracking on a smoothed validation criterion. The normalization, loss criterion, learning-rate schedule, training-window length, and integration scheme were each selected by a dedicated controlled comparison rather than by convention, and are reported as ablations in Section V-C.

2) *Data Splits*: Three complementary splits are employed. First, a stratified four-fold cross-validation holds out one trial per maneuver class per fold, 12 training and 4 validation trials each, so that every reported generalization figure is an average over class-balanced held-out maneuvers. Second, a leave- $r$ -repeats-out grid with  $r = 1, 2, 3$ , four folds each, at a matched 3000-epoch budget, traces the learning curve from 4 to 12 training trials under a consistent protocol. Third, the deployment model is fitted on all 16 trials with the cross-validation statistics serving as its unbiased accuracy estimate.

3) *Evaluation Discipline*: All evaluations roll the model open loop from the true initial state over each validation trial’s complete, untruncated duration, up to three times longer than the training windows, and report errors in physical units. Errors are decomposed into the moving region, the reverse subset, and within- versus beyond-training-horizon segments.

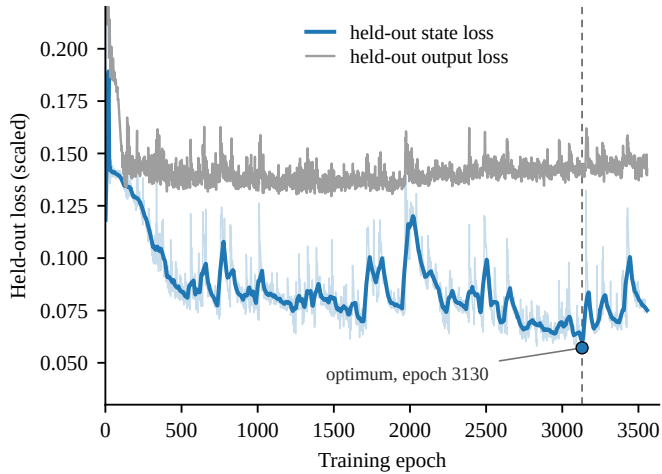


Fig. 4. Convergence of the held-out losses on one cross-validation fold. The blue state loss, shown raw and smoothed, bottoms at the marked optimum, epoch 3130; the gray output loss plateaus. Deployment fits are capped at 3200 epochs.

Model selection never relies on any inference-time state limiter; the comparison of limiters is itself a result, reported in Section V-B. Finally, run-to-run seed variability is treated as a noise floor to be measured, not a lottery to be exploited. Repeated trainings established a seed-induced coefficient of variation of approximately 2% on the moving-region velocity error and 3–4% on the yaw-rate error, and design decisions are accepted only when their effect exceeds this floor; candidate selection is otherwise resolved by simplicity or physical reasoning.

### C. Parking-Simulator Deployment

The closed-loop evaluation embeds the learned models in an interactive parking simulator driven by a production-representative planning stack: a Hybrid A\* lattice search [11] with Reeds–Shepp expansion [16], an optimization-based trajectory refinement [17], and a predictive steering tracker, detailed in the released simulator. Two principles govern the integration. First, the planner keeps its internal kinematic-bicycle model [18], as in a real vehicle; only the executed dynamics are exchanged for the learned plant, and closed-loop tracking absorbs the difference. Second, a command interface translates the tracker’s speed and steering commands into the production command set  $\{d_g, \tau_m^*, a_x^*, \delta_{sw}^*\}$  through a gear state machine and a longitudinal controller. The gear logic follows the field-test evidence that all 72 recorded direction changes shift reverse-to-drive at standstill without passing through neutral; park pins the states at zero for the parking pawl, while neutral forces  $\tau_m^* \equiv 0$  (Fig. 2). The longitudinal controller adds a brake-hold that raises the commanded deceleration to standstill, necessary because the learned plant reproduces the driveline creep torque that defeats a fixed gentle brake. Interface gains are tuned by coordinate descent on a 12-cell core; all robustness grids in Section V-F use held-out scenarios never seen during tuning.

The learned plant runs in the browser as a numerical port of the reference implementation, verified equivalent over

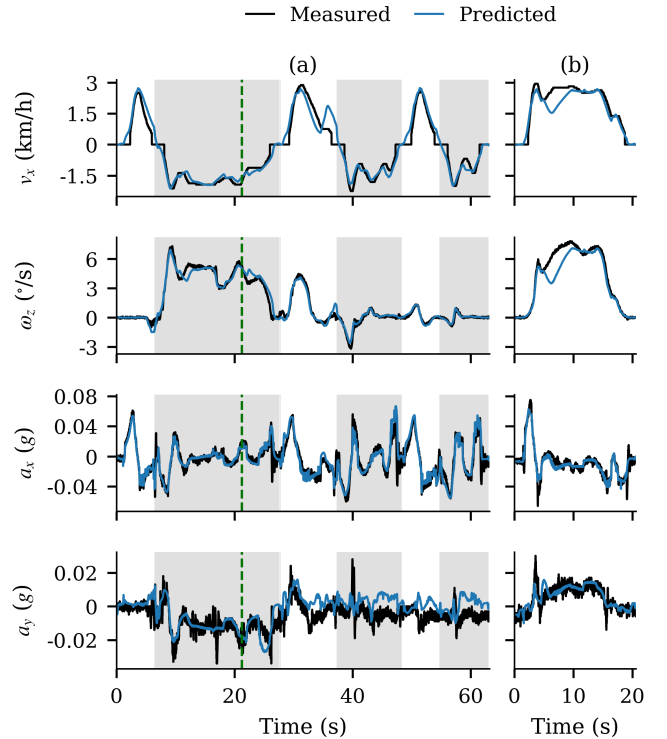


Fig. 5. Open-loop rollout on two held-out validation maneuvers of the canonical fold: (a) the multi-segment park-in and (b) the single-segment park-out, comparing measured and predicted  $v_x$ ,  $\omega_z$ ,  $a_x$ , and  $a_y$ . Rows share axes and the two maneuvers share a common time scale; shaded bands mark reverse-gear segments, and the green dashed line marks the training-window horizon.

TABLE I  
FOUR-FOLD CROSS-VALIDATION ON HELD-OUT MANEUVERS

Fold	$v_x$ [(km/h) <sup>2</sup> ]	Rev. $v_x$ [(km/h) <sup>2</sup> ]	$\omega_z$ [(°/s) <sup>2</sup> ]
0	0.057	0.051	0.162
1	0.095	0.040	0.201
2	0.121	0.065	0.575
3	0.160	0.072	0.439
mean $\pm$ std	$0.108 \pm 0.038$	$0.057 \pm 0.012$	$0.344 \pm 0.170$

recorded, closed-loop, and randomized command streams to floating-point precision, with each NARX submodel fed its true command history through a per-maneuver ring buffer.

## V. RESULTS AND DISCUSSION

### A. Open-Loop Validation

Table I reports the four-fold cross-validation on the complete held-out maneuvers in the moving region. The velocity MSE of  $0.108 \pm 0.038$  (km/h)<sup>2</sup> is a root-mean-square error of about 0.33 km/h on a signal reaching only 3 km/h. In the open-loop rollouts of Fig. 5, the shaded reverse segments are tracked as closely as the forward bursts.

The spread across folds has an identifiable origin. The one-step prediction errors are essentially identical across folds, so the spread emerges only under multi-step rollout, where occasional transient excursions at velocity transitions compound. Retraining the fold-1 model under three further random

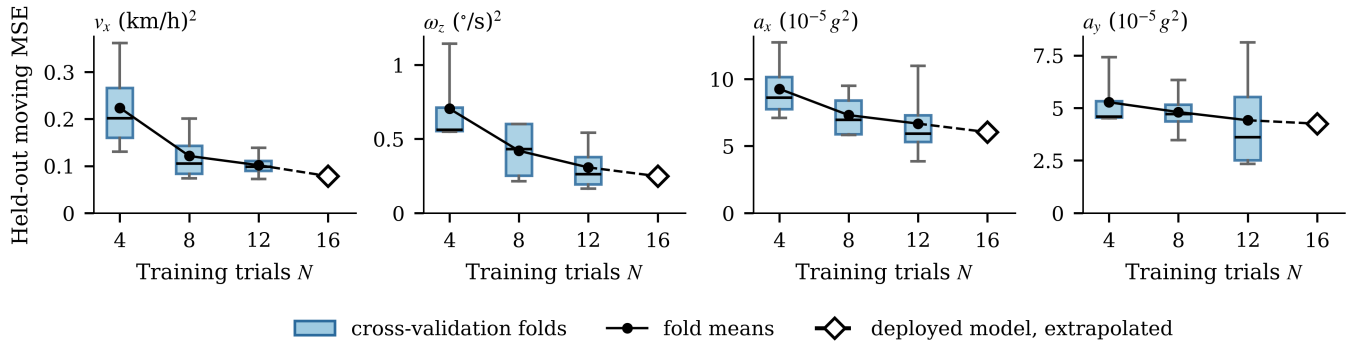


Fig. 6. Generalization versus training-set size under leave- $r$ -repeats-out cross-validation. Boxes span the four folds at each training-set size, and the solid line connects the fold means; the diamond marks the all-16 deployment model, whose held-out error is extrapolated by a power-law fit of the fold means because no held-out trial remains, and the dashed segment extends that fit.

seeds on the same split yields  $0.089 \pm 0.019$  (km/h)<sup>2</sup>, a within-split seed spread of the same order as the across-fold spread. The cross-validation variance therefore reflects training stochasticity compounding through the open-loop rollout, not differences in maneuver difficulty between folds.

Figure 6 places these results on the learning curve from the leave- $r$ -repeats-out grid: under the matched 3000-epoch protocol the velocity MSE falls monotonically from 4 to 12 training trials and is still descending at the data boundary. The model is therefore data-limited rather than capacity-limited, so further repetitions would improve accuracy directly, while the achieved level already suffices for the closed-loop application of Section V-F. Long-horizon behavior is likewise bounded: over complete maneuvers up to three times the training window the full-trajectory errors reach  $0.172$  (km/h)<sup>2</sup> and  $0.363$  (°/s)<sup>2</sup> without divergence, and the beyond-horizon segments are predicted no worse than those within the training window.

### B. The Physics-Informed Loss Replaces the Inference Limiter

The parent model [4] enforces physical plausibility through a hard state limiter applied at inference, deliberately keeping such clamping out of training; the physics-informed formulation of Section II-C inverts this philosophy. On the same trained model over the held-out maneuvers, adding the gear-conditioned kinematic limiter at inference changes the moving-region velocity error by under 3%, from  $0.160$  to  $0.156$  (km/h)<sup>2</sup>, and leaves the reverse-velocity and yaw-rate errors unchanged, all within the seed-noise floor, because the training losses (5)–(6) have already confined the dynamics to the admissible region. The limiter is therefore redundant, and removing it spares a per-step branch in the real-time loop. Its yaw envelope would in any case demand care: it must clamp the reconstructed yaw rate of (4), and clamping the residual channel directly pins it to the kinematic manifold, so the rollout diverges.

### C. Design Ablations

Every major design decision was resolved by a controlled comparison under the evaluation protocol of Section IV-B;

TABLE II  
DESIGN ABLATIONS ON HELD-OUT MANEUVERS

Axis	Option	$v_x$ [(km/h) <sup>2</sup> ]	$\omega_z$ [(°/s) <sup>2</sup> ]
Normalization	clipped min-max <sup>†</sup>	0.202	0.691
	plain min-max	<b>0.201</b>	0.716
	z-score	0.243	<b>0.618</b>
Loss (at its best LR)	MAE <sup>†</sup>	<b>0.163</b>	<b>0.657</b>
	MSE	0.173	0.701
	log-cosh	0.248	0.773
LR schedule	cosine <sup>†</sup>	<b>0.196</b>	0.699
	const.	0.202	<b>0.691</b>
Training window $L$	2121 (no padding) <sup>†</sup>	<b>0.079</b>	<b>0.280</b>
	3435 (10% padding)	0.103	0.327
	6390 (39% padding)	0.092	0.319

Each axis varies one factor with the others held at a stage-specific baseline, so values compare only within an axis. The best value in each column is in bold; <sup>†</sup>marks the option carried into the deployed model.

Table II consolidates the principal tuning axes, all evaluated on complete held-out maneuvers in the moving region.

1) *Robust Normalization and Loss*: Clipping each channel to its 0.5th–99.5th percentiles before min-max scaling is the deployed normalization, chosen to keep the scaled signals bounded: it ties plain min-max on velocity and trails only z-score on yaw, and z-score is rejected for the velocity penalty it pays on the priority variable (Table II). The deployed mean absolute error is the most accurate loss at its best learning rate and, by a wide margin, the smoothest to train, its late-training variation under 1% against 2.6% for MSE. The learning rate is the principal instrument for the velocity-yaw trade, since raising it improves the velocity at the expense of the yaw; the deployed cosine schedule sits at the velocity-favoring end at  $2 \times 10^{-3}$ , its yaw within the seed-noise floor of the constant schedule. The schedule rows of Table II isolate the schedule shape at a reduced learning rate.

2) *Short Training Windows Generalize Best to Long Roll-outs*: Although every evaluation rolls out over complete maneuvers of up to 6390 steps, training on the shortest 2121-step windows yields the best full-trajectory and even beyond-horizon accuracy, at a third of the per-epoch cost of full-length sequences, which spend 39% of their computation on

TABLE III  
ASSEMBLED-CHAIN FIDELITY LADDER

Configuration	$v_x$ [(km/h) <sup>2</sup> ]
All channels measured (reference)	0.059
Assembled chain, signal-fitted 1 s NARX brake	0.069
Assembled chain, consequence-tuned 1 s NARX brake	0.055 <sup>†</sup>
Monolithic NSS on commands, no submodels	0.130
Static affine actuator maps, no dynamics	0.375

<sup>†</sup>Deployed configuration.

padding. The cause is data diversity: the shortest window tiles the 12 training trials into 29 distinct training sequences whose gradients sample every maneuver phase, whereas the longer windows reduce the corpus to 12 to 18 padded sequences that generalize worse. Backpropagating through a longer horizon does not substitute for gradient diversity.

### 3) The Physics-Residual Readout Sharpens the Velocity:

Reading the yaw rate as a residual on the kinematic-bicycle prior of (3), rather than predicting it directly, lowers the moving-region velocity error by 27% and the yaw-rate error by 14% against an otherwise identical six-layer network. That the velocity gains more, though the readout acts on the yaw, follows from the coupling of (3): anchoring the yaw to its kinematic value spares the network from reproducing the motion the prior already explains and feeds the sharper yaw back into the velocity rollout through the shared state. The readout is retained in every deployed model.

### 4) Integration Order and Capacity Are Null Axes:

Replacing the forward-Euler integration in (2b) by midpoint or fourth-order Runge–Kutta changes the validation metrics by under 1% while costing 1.7 and 3.1 times the training wall clock, so the cheapest scheme is the correct engineering choice. Capacity behaves analogously: the selected six-layer state network outperformed both smaller variants and modernized alternatives, namely augmented latent states and residual connections with layer normalization, which overfit the 16-trial corpus.

## D. Actuator Submodel Selection

Actuator selection on the deployment model is evaluated at two closed-loop levels, both scored by the full-trajectory velocity MSE against the all-measured reference: a per-channel level that substitutes each candidate alone with all other channels measured (Fig. 7), and an assembly level that activates all submodels at once, summarized as a fidelity ladder in Table III.

### 1) Signal Fidelity Does Not Predict Closed-Loop Value:

The Phase-A fidelity screen and the end-to-end criterion disagree sharply. Across the 15 channel–architecture pairs of the three deployed channels, candidates at channel-best signal fidelity span chained velocity errors from near the all-measured reference to a 50-fold degradation, and the two criteria correlate at only +0.07 (Fig. 7): the drive channel’s highest-fidelity fit destabilizes the chain, while a long-memory brake fitted to the recorded signal, though it halves the hold-region pressure error, degrades the chain because

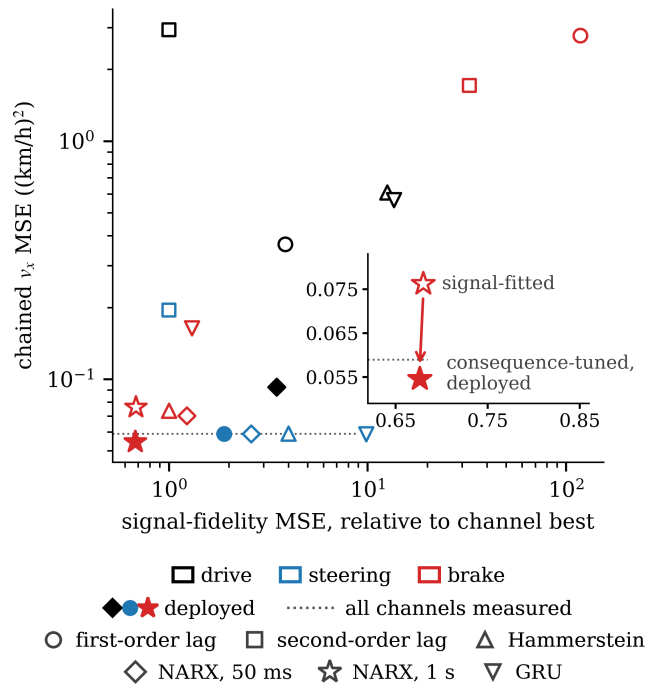


Fig. 7. Signal fidelity versus end-to-end closed-loop value for the command-only candidates of the three deployed channels; each point substitutes one candidate into the chain with all other channels measured. The two stars are the 1 s NARX brake before and after consequence-level co-tuning, and the inset magnifies its crossing of the reference at unchanged signal fidelity.

its learned hold transients fall where pressure errors carry velocity consequences. Submodels for closed-loop simulation must therefore be selected in the closed loop, and fidelity gains on autonomously actuated components warrant suspicion.

### 2) State Dependence Differs Across Channels:

Whether actuator dynamics depend on the vehicle state is answered per channel, and the answer differs. The drive channel benefits from a uniform state interface, cutting its per-channel error by a third and reflecting a torque response that varies with speed and gear; the brake is best modeled from commands alone, every state-aware variant losing in the assembled chain; and the steering channel is dynamically decoupled at parking speeds, so its one-parameter lag is chosen for simplicity. Closed-loop fine-tuning narrows a state-aware submodel’s identification-to-deployment gap but neither reverses an input-set disadvantage nor transfers across assemblies, so the deployed drive submodel is the identification-time one.

### 3) Consequence-Level Co-Tuning and the Value of Structure:

With every submodel active, the assembled chain is the governing criterion, stricter than signal fidelity or per-channel substitution because submodel errors interact through the shared vehicle state; its gap from the all-measured reference in Table III is the cost of replacing every measured signal by its submodel. The envelope stress study of Section III-B shows the input-domain clamp is the active regulator under out-of-domain commands, the output clamp a zero-cost backstop.

The long-memory failure above is a property of the training objective, not of memory itself. Fine-tuning the 1 s NARX end-to-end, by backpropagating the blind-zone-masked velocity

loss through a differentiable replica of the frozen chain into the brake weights alone, reverses the verdict. The co-tuned sub-model reaches  $0.055 \text{ (km/h)}^2$  full-trajectory and  $0.043$  in the moving region, against  $0.059$  and  $0.049$  for the 50 ms NARX under identical runtime, retaining the halved hold-region pressure error that signal-level training could not convert into closed-loop value (Fig. 7). The consequence loss weighs pressure errors by their effect on the vehicle state, a learned soft masking that outperforms an explicit hard mask. The full-trajectory figure dips below the all-measured reference, a co-adaptation to the vehicle model’s biases rather than accuracy beyond measurement, while the masked moving-region error stays above its  $0.037$  reference; signal-level fine-tuning never reversed an input-set disadvantage, whereas consequence-level co-optimization reversed an architecture-level one.

Two baselines without submodels bound the value of the chain’s structure in Table III. Static affine calibrations inflate the velocity error to nearly 7 times the deployed chain, and retraining the NSS on commanded inputs, absorbing the actuators with no submodels, reaches 2.4 times: the two-dimensional vehicle state carries no actuator memory, so a command-driven network has nowhere to store the torque build-up, hold pressure, and release latency that the submodels hold explicitly in their command histories. The modular chain is the accuracy-optimal arrangement of the same information.

The accuracy margin, however, is not the principal argument for the decomposition. The subsystems of an automated-parking stack evolve on independent schedules, and the modular chain absorbs a brake, steering-rack, or power-steering change by re-identifying the affected submodel alone, reusing the NSS and the other channels unchanged, whereas a monolithic model entangles every subsystem and forces a complete re-collection and retraining. Modularity thus converts vehicle-level retraining into component-level recalibration, which matters more than accuracy for sustained closed-loop use.

### E. Standardized Fidelity of the Deployed Chain

The mean-square errors of the fidelity ladder quantify accuracy in physical units but give no standardized measure of how closely the deployed plant reproduces the instrumented vehicle. The assembled command-to-vehicle chain is therefore additionally assessed under ISO/TS 18571 [19], an objective-rating metric that scores the correlation between a measured and a simulated time history, combining corridor, phase, magnitude, and slope sub-ratings into a single zero-to-one rating graded Excellent, Good, Fair, or Poor. From the recorded command stream the chain predicts four channels,  $v_x$ ,  $\omega_z$ ,  $a_x$ , and  $a_y$ , each rated against its measured counterpart over the complete maneuver across all 16 field tests. The rating is reported in two forms: the measured acceleration and yaw-rate signals carry wheel-speed and inertial-sensor noise that the smooth model neither reproduces nor should, and because the slope sub-rating is sensitive to it, this noise depresses the rating without reflecting model error. ISO/TS 18571 accordingly prescribes identical conditioning of both signals [19], so a 5 Hz zero-phase low-pass is applied to measured and predicted alike, with the raw rating retained alongside for transparency.

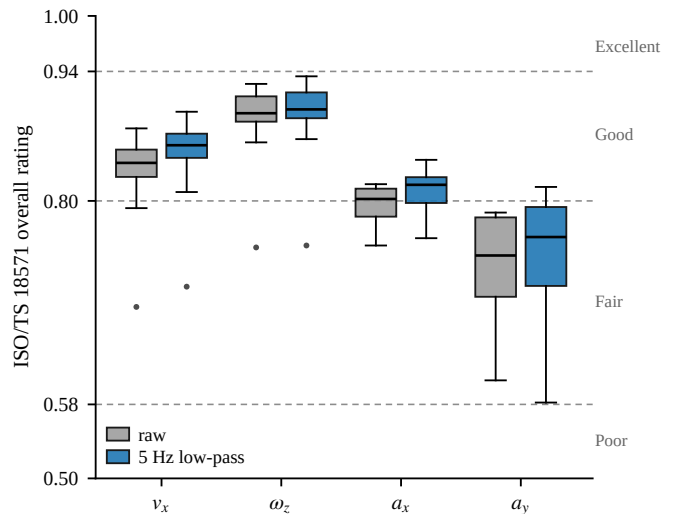


Fig. 8. Objective rating of the deployed command-to-vehicle chain against the measured field tests under ISO/TS 18571, per channel over the 16 maneuvers. Each box spans the 16 maneuver ratings; every maneuver is scored both raw and after an identical 5 Hz zero-phase low-pass on the measured and predicted signals. Dashed lines mark the ISO/TS 18571 grade thresholds.

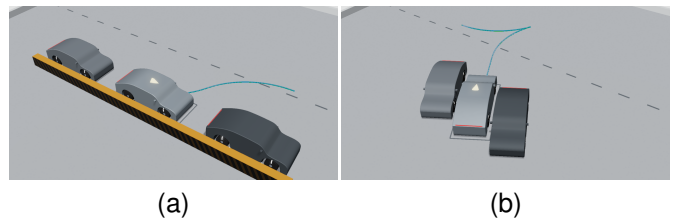


Fig. 9. Closed-loop execution of planned maneuvers by the NSS plant in the parking simulator: (a) the two-cusp parallel maneuver and (b) the one-cusp angled back-in maneuver. The planned path is drawn in green and the driven path in cyan; the two nearly coincide.

As Fig. 8 shows, the deployed chain attains Good ratings on the two state variables,  $v_x$  at  $0.83$  and  $\omega_z$  at  $0.89$ , and ranges from the Good–Fair boundary at the longitudinal acceleration  $a_x$ ,  $0.80$ , to Fair at the lateral acceleration  $a_y$ ,  $0.72$ , averaging  $0.81$  raw and  $0.82$  filtered across the four channels. The phase sub-rating is near unity throughout, while the slope sub-rating is the common limiter, consistent with the residual sensor noise that the 5 Hz conditioning partly relieves. The low  $v_x$  and  $\omega_z$  outliers come from the single maneuver with the largest open-loop velocity excursion at its motion-direction transitions, yet its ratings remain within the Fair band. Parking confines the acceleration channels to small-amplitude, low signal-to-noise dynamics, most acutely in the lateral axis, so their lower ratings relative to the state variables are expected, and that they remain Fair indicates the chain captures their essential character. These ratings characterize the reconstruction fidelity of the deployed all-16-maneuver model; held-out generalization is reported separately by Table I.

### F. Closed-Loop Evaluation in the Parking Simulator

The test of a vehicle model intended for simulation is whether a complete planning and control stack can park the car

TABLE IV  
CLOSED-LOOP EXECUTION OVER THE SCENARIO AND ROBUSTNESS  
GRIDS

	Kinematic	NSS <sup>†</sup>
Completed maneuvers	31/31	31/31
Goal error, mean [cm]	1.0	4.5
Goal error, median [cm]	0.8	3.5
Goal error, max [cm]	2.3	10.0
Driven clearance, mean [cm]	33.0	27.6
Cells under the 20 cm sensor floor	0	10
Held-out axes, NSS plant; goal error mean/med/max [cm]		
Obstacle skew $\pm 5^\circ$ (26 cells)	5.1 / 4.9 / 10.1	
Start jitter $\pm 0.25$ m, $\pm 3^\circ$ (52)	7.6 / 4.9 / 114.8	
Tighter slots, $-7.5$ cm (27)	9.0 / 4.5 / 105.3	
Looser slots, $+7.5$ cm (34)	18.4 / 4.8 / 463.9	

<sup>†</sup>Deployed execution plant.

through it. Table IV compares executed maneuvers over the deterministic 36-cell scenario grid, spanning three bay types, two approach directions, three difficulty tiers, and the lane barrier present or absent, under the ideal kinematic bicycle and the learned plant chain. The plan is identical in both, so the comparison isolates the cost of realistic dynamics.

Under the learned dynamics every plannable maneuver completes, parking to a median goal error of 3.5 cm against the kinematic plant’s idealized 0.8 cm, centimeter-level accuracy through real actuator lag, drivetrain creep, and brake-hold, executed in real time in the browser (Fig. 9). This required the longitudinal control of Section IV-C; without it the open-loop replay of the planned speed profile diverges, exactly as a real vehicle drifts from a clock-indexed plan. Under the same plan and controller, the learned dynamics stretch each maneuver some 15–18% beyond the kinematic execution (Fig. 10), yet the controller holds both to the same parked pose, while 10 cells in the tightest tiers finish below the 20 cm ultrasonic clearance floor the kinematic execution maintains by construction.

This clearance erosion is a controller-level trade, not a model deficiency. The predictive tracker cuts each corner slightly inside the plan, holding landing accuracy under 5 cm while shrinking the swept clearance, and disabling the feedback reverses the balance. The trade is fundamental to executing a kinematic plan on realistic dynamics; its production resolutions, replanning at junctions or clearance-aware tracking, lie beyond this paper’s scope, and the grid is reported with the trade visible rather than tuned away.

The lower block of Table IV probes overfitting of the interface tuning: the gains tuned on the 12-cell core are evaluated on a 252-cell extended grid of obstacle, start-pose, and slot-width perturbations never seen during tuning. The typical held-out cell parks at core-grid accuracy, with no cell changing solvability between the two plants; degradation is a tail phenomenon, five of the 139 plannable cells exceeding 20 cm where long brake-hold phases meet far-off-nominal geometry, the worst a loosened-slot topology that drives the command interface into a livelock far from the goal. These tails proved sensitive to the brake submodel: an intermediate deployment with a less accurate brake doubled the tail count

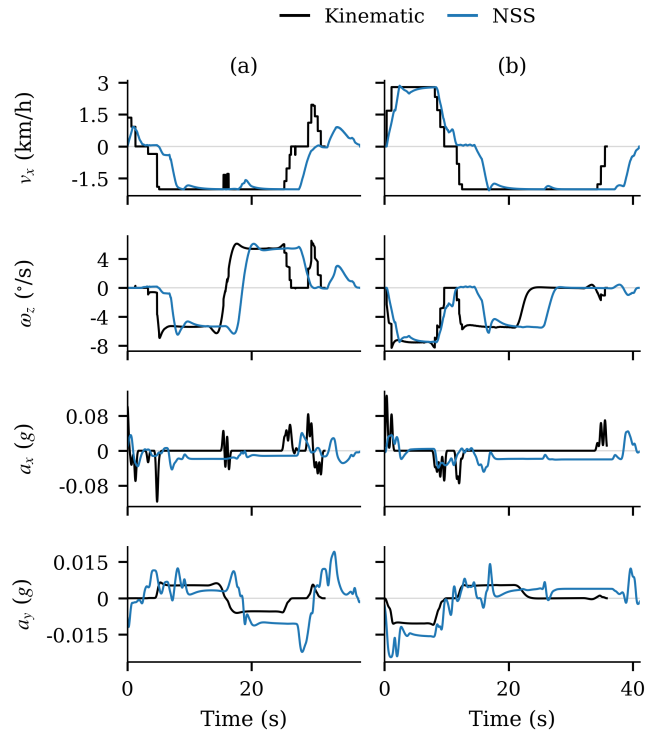


Fig. 10. Vehicle-state trajectories under the ideal kinematic plant and the NSS plant for the two maneuvers of Fig. 9: (a) the two-cusp parallel maneuver and (b) the one-cusp angled back-in. An identical plan and predictive controller drive both plants, so the difference isolates the plant dynamics. The two columns share a common time scale, and  $a_x$  and  $a_y$  are shown with a short smoothing window.

under identical gains, identifying the plant, not the controller tuning, as the binding factor for held-out robustness.

Beyond the gross motion, the learned plant carries the measured signal characteristics of the instrumented vehicle into the virtual phase, as the acceleration channels of Fig. 10 show. Where the kinematic plant emits only the accelerations its idealized motion implies, the NSS plant reproduces them as the on-board inertial sensor reports them, with the offset and attitude coupling that sensor mounting and load transfer introduce and the point-mass idealization omits. A parking controller consuming these signals, for ride-comfort shaping, grade or load compensation, or stop detection, can thus be tuned against realistic measurements before the target vehicle is instrumented.

## VI. CONCLUSION

This study develops a physics-informed neural state-space model tailored for the parking-regime dynamics of a production battery-electric sedan, identified entirely from field-test maneuvers and carried through to a real-time closed-loop deployment. By favoring a data-driven formulation grounded in physics over a fully parameterized description, this work captures the actuator lag, drivetrain creep, and direction reversals that the kinematic idealization omits at parking speeds. The gear-conditioned velocity constraint and the physics-residual yaw readout divide the labor between physics and

learning, so that imposing the physical constraints during training makes the customary inference-time state limiter redundant. The accompanying actuator study shows that a submodel must be judged inside the deployed assembly rather than by its signal fidelity, and that tuning the brake on its velocity consequence reverses the verdict reached against the long-memory architectures at the signal level.

The model generalizes to held-out maneuvers in fully open-loop simulation, and, despite being identified from only 16 field tests, the assembled command-to-vehicle chain earns Good ratings on the vehicle states under the ISO/TS 18571 objective rating metric. Embedded as the real-time plant of an interactive simulator, it enables a production-representative planning stack to park the vehicle through the learned dynamics. Because the model is identified entirely from field-test logs of the target vehicle rather than from a parameterized dynamics description, a simulator built around it can pre-calibrate an automated-parking planning and control stack in the virtual development phase without the manufacturer's proprietary chassis and actuator parameters. Future efforts will focus on broadening the single-vehicle data scale and extending the model to a wider range of road surface conditions, such as varying slopes and road adhesion coefficients. A further step is to unify this parking-regime model with the forward-driving dynamics of its precursor [4] into a single neural state-space model spanning the full speed envelope.

#### ACKNOWLEDGMENT

The authors would like to express their gratitude to Mrs. Grace (Shenghan) Gao for her guidance and advice on the writing and grammatical aspects of this paper.

#### REFERENCES

- [1] S.-Y. Oh and Y. Yim, "Modeling of vehicle dynamics from real vehicle measurements using a neural network with two-stage hybrid learning for accurate long-term prediction," in *Proc. IEEE Int. Symp. Comput. Intell. Robot. Autom. (CIRA)*, Monterey, CA, USA, 1999, pp. 83–88.
- [2] N. A. Spielberg, M. Brown, N. R. Kapania, J. C. Kegelmann, and J. C. Gerdes, "Neural network vehicle models for high-performance automated driving," *Sci. Robot.*, vol. 4, no. 28, Art. no. eaaw1975, 2019.
- [3] X. Nie, C. Min, Y. Pan, K. Li, and Z. Li, "Deep-neural-network-based modelling of longitudinal-lateral dynamics to predict the vehicle states for autonomous driving," *Sensors*, vol. 22, no. 6, Art. no. 2013, 2022.
- [4] P. Song, L. Zheng, G. Tian, and L. Zhang, "Data-driven vehicle dynamics: Neural network modeling for system identification and prediction in driver assistance control," *Automot. Innov.*, vol. 8, no. 1, pp. 46–58, 2025.
- [5] R. T. Q. Chen, Y. Rubanova, J. Bettencourt, and D. Duvenaud, "Neural ordinary differential equations," in *Proc. Adv. Neural Inf. Process. Syst. (NeurIPS)*, Montreal, QC, Canada, 2018, pp. 6571–6583.
- [6] D. Masti and A. Bemporad, "Learning nonlinear state-space models using autoencoders," *Automatica*, vol. 129, Art. no. 109666, 2021.
- [7] M. Forgione and D. Piga, "Continuous-time system identification with neural networks: Model structures and fitting criteria," *Eur. J. Control.*, vol. 59, pp. 69–81, 2021.
- [8] M. Raissi, P. Perdikaris, and G. E. Karniadakis, "Physics-informed neural networks: A deep learning framework for solving forward and inverse problems involving nonlinear partial differential equations," *J. Comput. Phys.*, vol. 378, pp. 686–707, 2019.
- [9] J. Chrosniak, J. Ning, and M. Behl, "Deep dynamics: Vehicle dynamics modeling with a physics-constrained neural network for autonomous racing," *IEEE Robot. Autom. Lett.*, vol. 9, no. 5, pp. 5292–5297, 2024.
- [10] A. Baier, Z. Boukhers, and S. Staab, "Hybrid physics and deep learning model for interpretable vehicle state prediction," arXiv:2103.06727, 2022. [Online]. Available: <https://arxiv.org/abs/2103.06727>
- [11] D. Dolgov, S. Thrun, M. Montemerlo, and J. Diebel, "Path planning for autonomous vehicles in unknown semi-structured environments," *Int. J. Robot. Res.*, vol. 29, no. 5, pp. 485–501, 2010.
- [12] J. Lian, W. Ren, D. Yang, L. Li, and F. Yu, "Trajectory planning for autonomous valet parking in narrow environments with enhanced hybrid A\* search and nonlinear optimization," *IEEE Trans. Intell. Veh.*, vol. 8, no. 6, pp. 3723–3734, 2023.
- [13] S. Hochreiter and J. Schmidhuber, "Long short-term memory," *Neural Comput.*, vol. 9, no. 8, pp. 1735–1780, 1997.
- [14] J. Sjöberg *et al.*, "Nonlinear black-box modeling in system identification: A unified overview," *Automatica*, vol. 31, no. 12, pp. 1691–1724, 1995.
- [15] K. Cho *et al.*, "Learning phrase representations using RNN encoder-decoder for statistical machine translation," in *Proc. Conf. Empirical Methods Natural Lang. Process. (EMNLP)*, Doha, Qatar, 2014, pp. 1724–1734.
- [16] J. Reeds and L. Shepp, "Optimal paths for a car that goes both forwards and backwards," *Pac. J. Math.*, vol. 145, no. 2, pp. 367–393, 1990.
- [17] X. Zhang, A. Liniger, and F. Borrelli, "Optimization-based collision avoidance," *IEEE Trans. Control Syst. Technol.*, vol. 29, no. 3, pp. 972–983, 2021.
- [18] P. Polack, F. Althé, B. d'Andréa-Novel, and A. de La Fortelle, "The kinematic bicycle model: A consistent model for planning feasible trajectories for autonomous vehicles?" in *Proc. IEEE Intell. Veh. Symp. (IV)*, Redondo Beach, CA, USA, 2017, pp. 812–818.
- [19] *Road Vehicles, Objective Rating Metric for Non-Ambiguous Signals*, Standard ISO/TS 18571:2024, International Organization for Standardization, Geneva, Switzerland, 2024.